remote sensing

MDPI

Article

A Novel Method to Identify the Spaceborne SAR Operating Mode Based on Sidelobe Reconnaissance and Machine Learning

Runfa Ma [1,2], Guodong Jin [1,2,*], Chen Song [3], Yong Li [1], Yu Wang [1] and Daiyin Zhu [1]

[1] The Key Laboratory of Radar Imaging and Microwave Photonics, Ministry of Education, Nanjing University of Aeronautics and Astronautics, Nanjing 211106, China; marunfa@nuaa.edu.cn (R.M.); limack@nuaa.edu.cn (Y.L.); wyu@nuaa.edu.cn (Y.W.); zhudy@nuaa.edu.cn (D.Z.)
[2] Nanjing University of Aeronautics and Astronautics Shenzhen Research Institute, Shenzhen 518063, China
[3] National Key Laboratory of Microwave Imaging Technology, Aerospace Information Research Institute, Chinese Academy of Sciences, Beijing 100190, China; songchen@aircas.ac.cn
* Correspondence: jinguodong@nuaa.edu.cn

Abstract: Operating mode identification is an important prerequisite for precise deceptive jamming technology against synthetic aperture radar (SAR). In order to solve the problems of traditional spaceborne SAR operating mode identification, such as low identification accuracy, poor timeliness, and limitation to main lobe reconnaissance, an efficient identification method based on sidelobe reconnaissance and machine learning is proposed in this paper. It can identify four classical SAR operating modes, including stripmap, scan, spotlight and ground moving target indication (GMTI). Firstly, the signal models of different operating modes are presented from the perspective of sidelobe reconnaissance. By setting the parameters differently, such as the SAR trajectory height, antenna length, transmit/receive gain and loss, signal–noise ratio, and so on, the feature samples based on multiple parameters can be obtained, respectively. Then, based on the generated database of feature samples, the initialized neural network can be pre-trained. As a result, in practice, with the intercepted sidelobe signal and the pre-trained network, we can precisely infer the SAR operating mode before the arrival of the main lobe beam footprint. Finally, the effect of SNR and the jammer's position on the identification accuracy is experimentally detailed in the simulation. The simulation results show that the identification accuracy can reach above 91%.

Keywords: synthetic aperture radar (SAR); operating mode identification; sidelobe reconnaissance; machine learning

Citation: Ma, R.; Jin, G.; Song, C.; Li, Y.; Wang, Y.; Zhu, D. A Novel Method to Identify the Spaceborne SAR Operating Mode Based on Sidelobe Reconnaissance and Machine Learning. *Remote Sens.* **2024**, *16*, 1234. https://doi.org/10.3390/rs16071234

Academic Editor: Dusan Gleich

Received: 29 January 2024
Revised: 14 March 2024
Accepted: 29 March 2024
Published: 31 March 2024

1. Introduction

Synthetic aperture radar (SAR), providing high-resolution two-dimensional images independent from daylight, cloud coverage, and weather conditions, has become an important means of intelligence acquisition [1–5]. Therefore, active jamming and anti-jamming technologies for SAR have become a hot topic in the field of radar electronic warfare [6–10]. Deception jamming is a common and efficient kind of active jamming [11,12]. However, in order to generate false targets with high fidelity in SAR images, some key parameters must be obtained first, and then the jamming signal which is coherent with the SAR signal in both range and azimuth direction can be generated [13–16]. At present, most of the parameter reconnaissance technologies use the intercepted SAR signals to acquire intra-pulse parameters such as bandwidth, frequency-modulated rate, and carrier frequency. The radar parameters and the range of illumination are set differently in different SAR operating modes, which means the risk level and adopted jamming methods for different operating modes are not the same. Therefore, the research of the spaceborne SAR operating mode identification is of great value.

Generally, classic and common SAR operating modes include stripmap, scan, and spotlight [17]. Spotlight SAR plays an important role in the military with its high resolution,

which is also the mode with the highest threat level. The method proposed in this paper has good extensibility and this paper will take the above modes (stripmap, scan, and spotlight) examples to carry out experiments without loss of generality. For stripmap SAR, with the movement of the SAR platform, the antenna remains in a consistent direction and illuminates the target area with a constant speed to obtain a continuous image [18–20]. The swath length of stripmap SAR only depends on the distance the satellite moves. The azimuth resolution is limited by the size of the antenna, and it cannot be better than half of the antenna length. Spotlight SAR adjusts the line of sight by controlling the azimuth beam direction of the antenna to make it always point to the target area. Therefore, it can improve the coherent accumulation time in azimuth, and thereby increase the synthetic aperture length, and finally obtain a much higher azimuth resolution [21–24]. However, spotlight SAR can only image a small area at a time and the beam coverage area is discontinuous. Scan SAR controls the antenna beam to successively point to several sub-swaths along the ground range direction [25–28]. Scan SAR obtains a much wider swath while degrading the azimuth resolution. The pattern of the beam illumination of the three SAR operating modes is shown in the figure below (Figure 1).

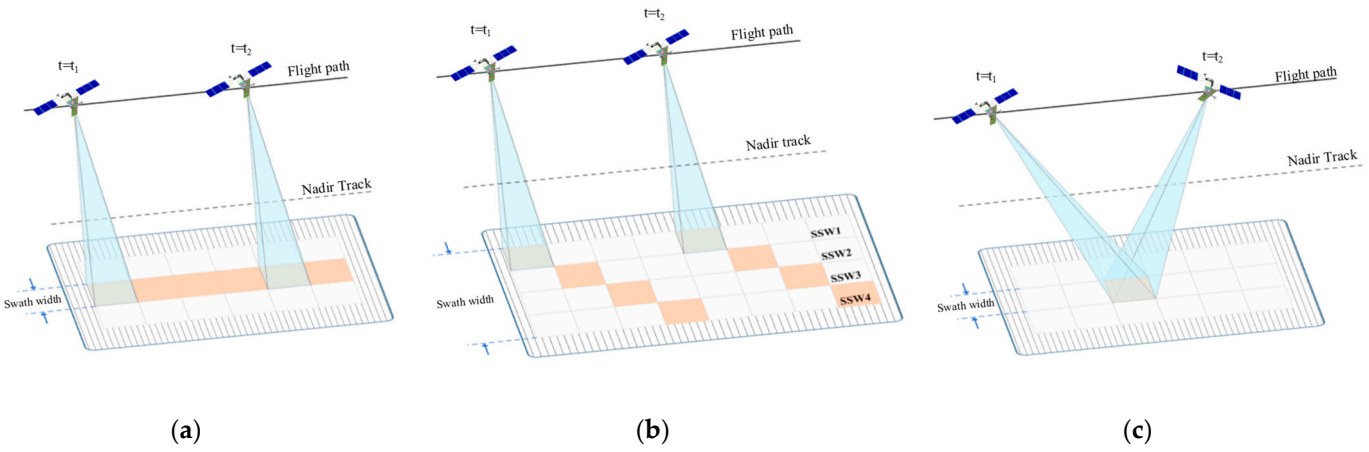

(**a**) (**b**) (**c**)

Figure 1. Illustration of different SAR operating modes, where 'SSW' is the abbreviation for sub-swath. (**a**) Stripmap SAR; (**b**) scan SAR; (**c**) spotlight SAR.

Aiming at solving the problem of SAR operating mode identification, researchers have made some important achievements in the last decade. The spaceborne SAR reconnaissance equation was established and the power curves of the received signal for stripmap and spotlight SAR were analyzed in [29], but the identification of the SAR operating mode was not further studied. The problem of the SAR operating mode identification was transformed into the extremum search of the sum of the power deviation squares between theoretical data and actual data in [30]. The genetic algorithm was used to obtain higher computing efficiency than conventional global search algorithms. However, local convergence may occur, so multi-station measurement could be employed to improve its stability, which means the cost of measurement will be increased. Furthermore, in [31], the Doppler history and the received power pattern of SAR signal were used to comprehensively identify the operating mode of the spaceborne SAR. Besides, the characteristics of the received azimuth power pattern in stripmap, spotlight, and sliding spotlight SAR were also summarized. Moreover, a spaceborne SAR operating mode recognition method based on deep learning was proposed in [32], which largely improved the identification speed and reduced the complexity of the process, but did not consider the noise and the acquirement of the a priori information. Currently, most of the relevant research studies are based on the main lobe signals. However, in practice, the jammer based on main lobe reconnaissance cannot provide overhead warning before the main lobe beam illuminates the target area. Besides, the traditional SAR operating mode identification method is to extract the signal features, and then identify the mode manually, which is inefficient and has poor anti-noise

performance. To this end, the proposed method solves the above problems by modeling the sidelobe reconnaissance signals and employing the neural network algorithm to perform fast and accurate identification [33,34].

Compared with the existing literature, the main advantages and contributions of this study can be summarized as follows:

1. The current spaceborne SAR operating mode identification methods are mainly based on main lobe reconnaissance, which has the disadvantages of poor real-time performance and low efficiency. To this end, the proposed sidelobe reconnaissance signal model in this paper is more universal and helps achieve overhead warning in advance;
2. Furthermore, we have discussed the effect of SNR and the jammer's position with detailed simulation experiments, and the results indicate that the performance of the proposed method is still desirable at low SNR and is hardly affected by the jammer's position. It shows that the method has good robustness and practicability;
3. Finally, considering the very low SNR problem resulting from sidelobe attenuation, the fractional Fourier transform (FrFT) algorithm is employed to estimate the frequency-modulated rate, and pulse compression is further adopted to enhance SNR equivalently.

The rest of this paper is organized as follows. Section 2 models the signal with a three-dimensional antenna pattern from the perspective of sidelobe reconnaissance, and further gives the complete SAR signal model. Section 3 introduces the fast identification algorithm for the SAR operating mode based on machine learning and shows the process of the dataset production. In Section 4, considering the effect of SNR, the position of the jammer, and the number of the accumulated pulses, detailed simulation experiments are carried out to verify the robustness of this method to these factors. In the end, a short conclusion is drawn in Section 5.

2. Signal Model of Sidelobe Reconnaissance

Spaceborne SAR achieves high azimuth resolution by forming a narrow beam in azimuth. When detecting only main lobe signals, the effective tracking time of the reconnaissance system will be very short due to the high speed of the SAR platform and the narrow beam in azimuth. Therefore, it becomes difficult to provide a SAR overhead warning and then start the jamming system timely. Considering the truth that spaceborne SAR usually has high emitting power and a low orbit, the receiving power of a sidelobe signal is high enough, which makes sidelobe reconnaissance possible. Besides, sidelobe reconnaissance has plenty of advantages, such as improving the discovery probability and detecting the target even earlier so as to increase the tracking time.

In this section, the three-dimensional antenna pattern is modeled and the complete radar equation of sidelobe reconnaissance is given. At present, antennas that are successfully applied to spaceborne SAR mainly include: the planar microstrip array antenna, parabolic antenna, and waveguide slot array antenna [35]. The antenna composition varies with its form. For example, a parabolic antenna is comprised of a reflector and a feed system, while a planar array antenna consists of an antenna array and a feed network. Considering that spaceborne SAR mostly uses a planar microstrip array antenna, this article will model the antenna pattern based on the planar array theory.

2.1. Radar Equation of Sidelobe Reconnaissance

The SAR signal intercepted by the ground-based jammer can be simplified as a periodic pulse string with Gauss white noise. In free space, the power density of the signal at the position of the jammer can be expressed as

$$S_e = \frac{P_t G_t(\varphi_A, \varphi_R)}{4\pi R^2 L_t}, \tag{1}$$

where P_t is the radar transmitting power; $G_t(\varphi_R, \varphi_A)$ is the transmitting gain of the antenna in the direction of the jammer; φ_A is the azimuth angle of the antenna pattern and φ_R is the range angle (the mathematical expressions of φ_A and φ_R in different operating mode will be deduced in detail, respectively, in Section 2.2); R is the distance between the spaceborne SAR and the ground-based jammer; and L_t is the transmitting loss of SAR, mainly including the feed line loss between the SAR transmitter and its antenna.

The effective area of the jammer antenna is given by

$$A_r = \frac{G_r \lambda^2}{4\pi}, \tag{2}$$

where G_r is the receiving gain of the jammer antenna in the direction of the spaceborne SAR (it is assumed that the jammer antenna is isotropic, hence it will be set as a fixed value in the experiment), and λ is the wavelength of the SAR signal.

In free space, the signal power at the jammer's location can be expressed as

$$P_{rf} = S_e A_r. \tag{3}$$

Furthermore, the signal power at the input-side of the jammer can be expressed as

$$P_r = \frac{P_{rf}}{L_r}, \tag{4}$$

where L_r is the receiving loss of the jammer, mainly including: the feed line loss between the jammer antenna and the input end, and the polarization mismatch loss between the jammer antenna and SAR signal.

Accordingly, the signal amplitude at the output-side of the jammer can be expressed as

$$A_s = \sqrt{\frac{P_t G_t(\varphi_A, \varphi_R) G_r \lambda^2}{(4\pi R)^2 L_t L_r} Z}, \tag{5}$$

where Z is the load impedance of the jammer.

2.2. Three-Dimensional Antenna Pattern

The modeling of the three-dimensional antenna pattern can be simplified as the multiplication of two two-dimensional planar patterns, namely the azimuth plane and the elevation plane. According to the planar array theory, assuming that the antenna ports are evenly distributed, when the aperture size of the antenna is much larger than the signal wavelength (generally more than four times), the antenna pattern of the azimuth plane and the elevation plane can be approximated as a 'sinc' function [36–38], and the three-dimensional antenna pattern in the form of amplitude can be expressed as

$$F(\varphi_A, \varphi_R) = \left| \sin c\left(\frac{D_A \sin \varphi_A}{\lambda}\right) \sin c\left(\frac{D_R \sin \varphi_R}{\lambda}\right) \right|, \tag{6}$$

where D_A is the equivalent azimuth antenna length, and D_R is the equivalent range antenna length; $\mathrm{sinc}(x)$ represents the normalized 'sinc' function.

As a result, the transmitting gain of the spaceborne SAR antenna in the direction of the jammer can be expressed as

$$G_t(\varphi_R, \varphi_A) = G_t(0,0) F^2(\varphi_A, \varphi_R), \tag{7}$$

where $G_t(0,0)$ is the gain peak of the main lobe beam, namely the transmitting gain when $\varphi_A = 0$ and $\varphi_R = 0$.

The above is a general model of a three-dimensional antenna pattern applicable to all operating modes of spaceborne SAR. The azimuth angle and range angle of the antenna pattern in different operating modes vary in different ways. Based on the two assumptions

of SAR uniform rectilinear motion and rectilinear geometry, we are going to deduce the azimuth angle and the range angle of stripmap, scan, and spotlight SAR, respectively. To start with, the geometric relationship of stripmap SAR is shown in the figure below (Figure 2).

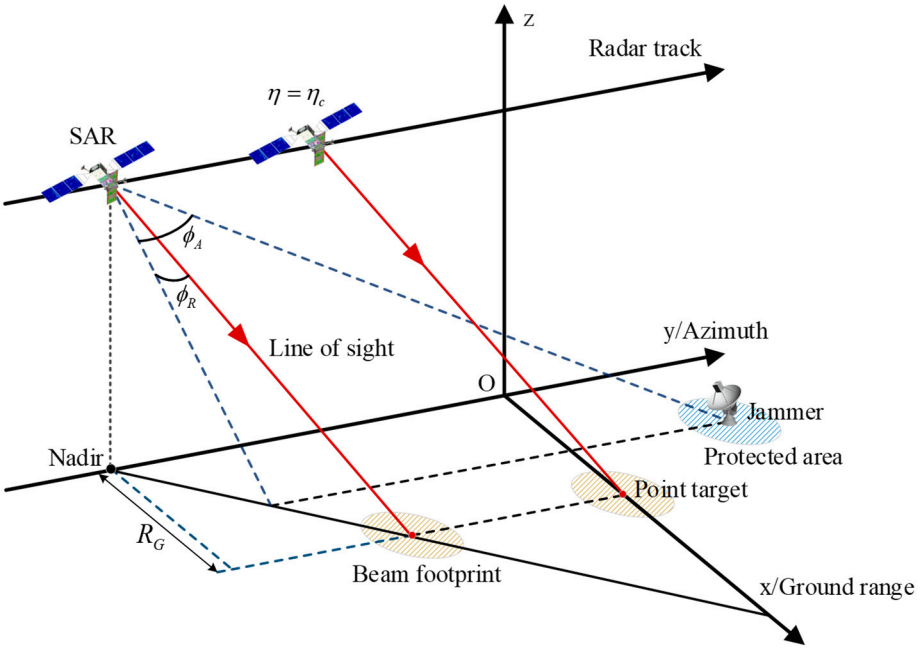

Figure 2. Geometric relationship of stripmap SAR, where $\eta = \eta_c$ denotes the beam center crossing time.

As shown in the figure above, the x-axis is defined as the direction of the ground range, the y-axis is defined as the velocity direction of spaceborne SAR, and the z-axis is perpendicular to the ground. Setting the coordinates of SAR as $R(0, V_r\eta, H)$, the coordinates of the point target on the ground as $A(R_G, 0, 0)$, and the coordinates of the jammer as $P(x_0, y_0, 0)$, when the SAR operates in stripmap mode, the azimuth angle and range angle of the antenna pattern can be expressed as

$$\phi_A = \arccos\left(\frac{x_0^2 + (y_0 - V_r\eta)(-V_r\eta_c x_0/R_G) + H^2}{\sqrt{x_0^2 + (y_0 - V_r\eta)^2 + H^2} \cdot \sqrt{x_0^2 + (V_r\eta_c x_0/R_G)^2 + H^2}}\right), \tag{8}$$

$$\phi_R = \arccos\left(\frac{R_G x_0 + (V_r\eta_c)^2 x_0/R_G + H^2}{\sqrt{R_G^2 + (V_r\eta_c)^2 + H^2} \cdot \sqrt{x_0^2 + (V_r\eta_c x_0/R_G)^2 + H^2}}\right), \tag{9}$$

where V_r denotes the equivalent velocity of the SAR platform; η is the slow time in the azimuth direction, and η_c is the beam center crossing time of the point target $A(R_G, 0, 0)$; H is the SAR platform height; R_G is the ground range from the point target $A(R_G, 0, 0)$ to the SAR trajectory.

As for scan SAR, we set the coordinates of SAR as $R(0, V_r\eta, H)$, the coordinates of the point target on the ground as $A(R_G, 0, 0)$, and the coordinates of the jammer as $P(x_0, y_0, 0)$, just the same as in the case of stripmap SAR. Since the observation swath contains several sub-swaths, the center of the beam footprint will be scanned along the center line of each sub-swath in turn. The geometric relationship of scan SAR is shown in the figure below (Figure 3).

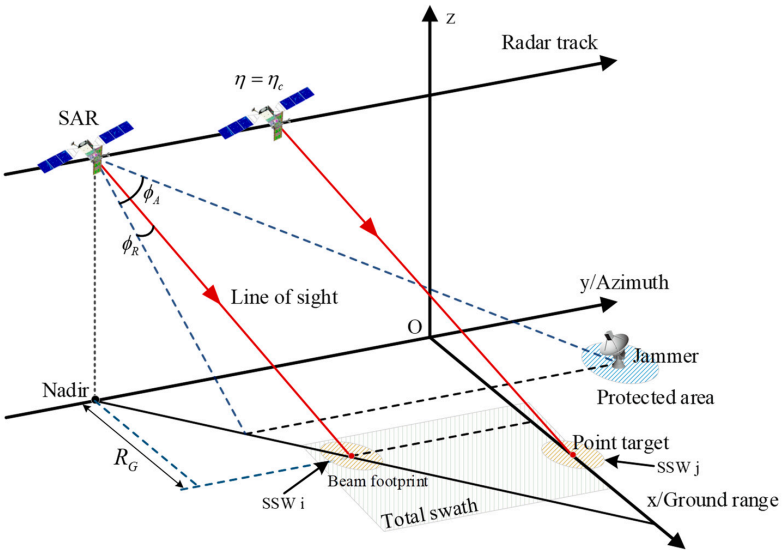

Figure 3. Geometric relationship of scan SAR, where SSW is the abbreviation for sub-swath.

After the deduction, the azimuth angle and range angle of the antenna pattern can be expressed as

$$\phi_A = \arccos\left(\frac{x_0^2 + (y_0 - V_r\eta)(-V_r\eta_c x_0/R_G(i)) + H^2}{\sqrt{x_0^2 + (y_0 - V_r\eta)^2 + H^2}\cdot\sqrt{x_0^2 + (V_r\eta_c x_0/R_G(i))^2 + H^2}}\right), \quad (10)$$

$$\phi_R = \arccos\left(\frac{R_G(i)x_0 + (V_r\eta_c)^2 x_0/R_G(i) + H^2}{\sqrt{(R_G(i))^2 + (V_r\eta_c)^2 + H^2}\cdot\sqrt{x_0^2 + (V_r\eta_c x_0/R_G(i))^2 + H^2}}\right), \quad (11)$$

where $R_G(i), i = 1, 2, 3, \ldots, N_s$ indicates the ground range of the center line of each sub-swath, and N_s is the number of the sub-swaths.

With regard to spotlight SAR, we set the coordinates of SAR as $R(0, V_r\eta, H)$, the coordinates of the point target on the ground as $A(R_G, 0, 0)$, and the coordinates of the jammer as $P(x_0, y_0, 0)$, just the same as in the case of stripmap SAR. The geometric relationship of spotlight SAR is shown in the figure below (Figure 4).

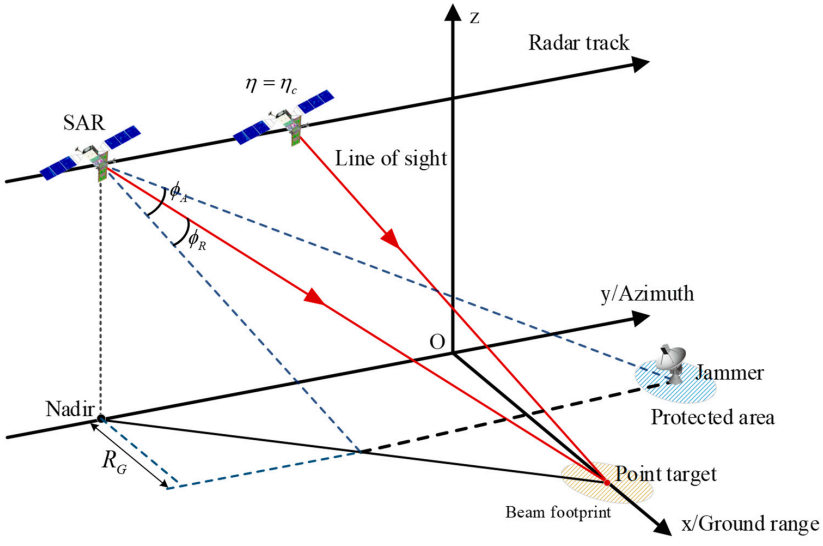

Figure 4. Geometric relationship of spotlight SAR.

As a result, the azimuth angle and range angle of the antenna pattern of spotlight SAR are deduced as follows

$$\phi_A = \arccos\left(\frac{x_0^2 + (y_0 - V_r\eta)(-V_r\eta x_0/R_G) + H^2}{\sqrt{x_0^2 + (y_0 - V_r\eta)^2 + H^2} \cdot \sqrt{x_0^2 + (V_r\eta x_0/R_G)^2 + H^2}}\right), \tag{12}$$

$$\phi_R = \arccos\left(\frac{R_G x_0 + (V_r\eta)^2 x_0/R_G + H^2}{\sqrt{R_G^2 + (V_r\eta)^2 + H^2} \cdot \sqrt{x_0^2 + (V_r\eta x_0/R_G)^2 + H^2}}\right) \tag{13}$$

2.3. Intercepted SAR Signal Model

Considering that spaceborne SAR generally transmits linear frequency-modulated (LFM) signals and such signals are easily intercepted, this article will conduct modeling based on LFM signals.

The SAR signal intercepted by the jammer can be expressed as

$$s(\tau, \eta) = A_s \cdot \mathrm{rect}\left(\frac{\tau - R(\eta)/c}{T_r}\right) \exp\left\{\mathrm{j}2\pi f_c[\tau - R(\eta)/c] + \mathrm{j}\pi K_r[\tau - R(\eta)/c]^2\right\}, \tag{14}$$

where τ denotes the fast time; c is the speed of light; T_r is the pulse duration; f_c is the carrier frequency; K_r is the linear frequency-modulated rate of LFM signal; and $R(\eta)$ is the distance between the spaceborne SAR and the jammer, according to the rectilinear geometry hypothesis, which can be expressed as

$$R(\eta) = \sqrt{x_0^2 + (V_r\eta - y_0)^2 + H^2}. \tag{15}$$

The spaceborne SAR signal demodulated by the jammer can be expressed as

$$s(\tau, \eta) = A_s \cdot \mathrm{rect}\left(\frac{\tau - R(\eta)/c}{T_r}\right) \exp\left\{-\mathrm{j}2\pi f_c R(\eta)/c + \mathrm{j}\pi K_r[\tau - R(\eta)/c]^2\right\}. \tag{16}$$

3. Fast Recognition Algorithm for SAR Mode

3.1. Method of Database Production

When conducting sidelobe reconnaissance, it is feasible to judge the SAR operating mode by observing the maximum value of SAR antenna gain and its variation trend, which can be represented by the variation trend of the amplitude peak value of received pulses [31,32]. Based on this viewpoint, this paper will mainly take the amplitude peak values of SAR pulses as the characteristic variable to identify the operating mode. Due to the uncertainty of both the start-up time of spaceborne SAR and the position of the point target, it will be difficult to intercept a bunch of SAR pulses that are long enough. In order to simulate a fairly real scene, when generating intercepted signals, the jammer is arranged at a position far away from the point target (about a few kilometers away), and the spaceborne SAR is set to start up before its beam footprint gets close to the target area. In addition, the number of pulses in a complete pulse bunch transmitted by the spaceborne SAR is set as no more than 1000, which helps the reconnaissance system to identify the SAR operating mode much faster and earlier. The two-dimensional signal data of each mode intercepted by the jammer are shown in the figure below (Figure 5).

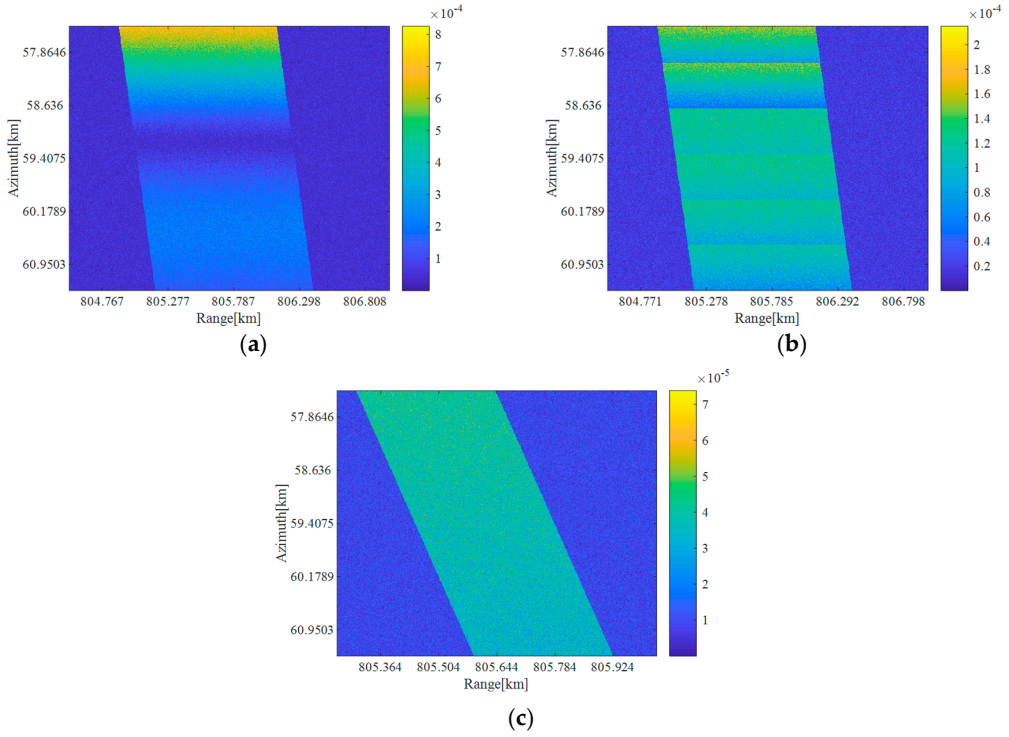

Figure 5. Amplitude of the intercepted signal of each mode (unit: Volt, SNR: 0 dB). (**a**) Stripmap SAR; (**b**) scan SAR; (**c**) spotlight SAR.

The sample generation method is as follows (the number of the accumulated pulses is set to 500 as an example): the amplitude peak values of 500 intercepted pulses are extracted to obtain a matrix whose size is 500 × 1. Both the matrix and its corresponding label (in the experiment, the labels for stripmap, scan, and spotlight are set as 0, 1, and 2, respectively) constitute a database sample. By changing system parameters, like the signal-to-noise ratio (SNR), the SAR operating mode, and other parameters, enough samples are generated in batches as the train set and the test set, respectively. According to the above method, the echo data in the above figure are respectively made into database samples, and the results are shown in the figure below (Figure 6).

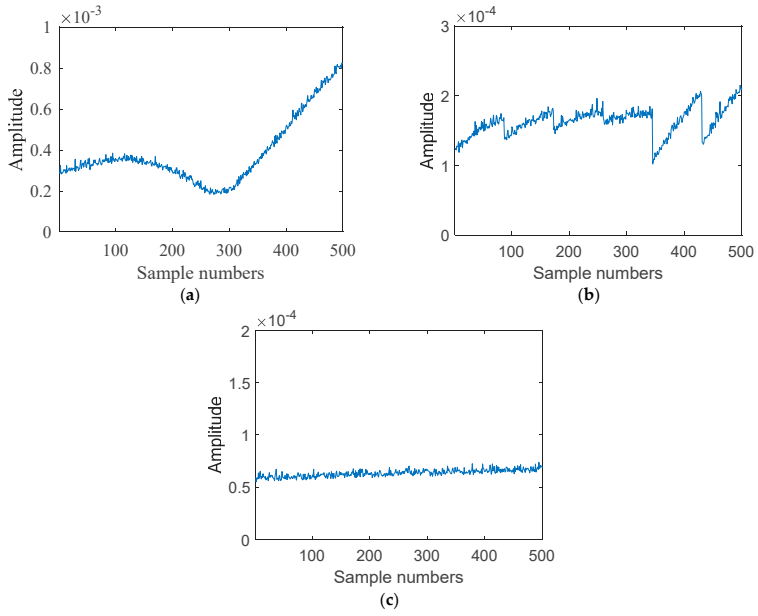

Figure 6. Samples of each mode. (**a**) Stripmap SAR; (**b**) scan SAR; (**c**) spotlight SAR.

As shown in the above figure, for a given jammer position, it can be clearly seen that the variation of the signal amplitude in different modes has its own characteristics. In this case, clearly, spotlight SAR goes through only a small portion of a sidelobe, while stripmap SAR and scan SAR go through about an entire sidelobe. This is because spotlight SAR usually has a longer synthetic aperture time. It is based on this feature that we can make good use of the characteristics of the antenna pattern to identify the SAR operating mode.

It should be noted that the samples in the above figure are generated under the same set of parameters. In fact, sometimes the signals intercepted from stripmap, scan, and spotlight SAR may be hard to identify. The following figure (Figure 7) shows two samples generated under two sets of parameters, which have similar characteristics that are difficult to identify for traditional methods.

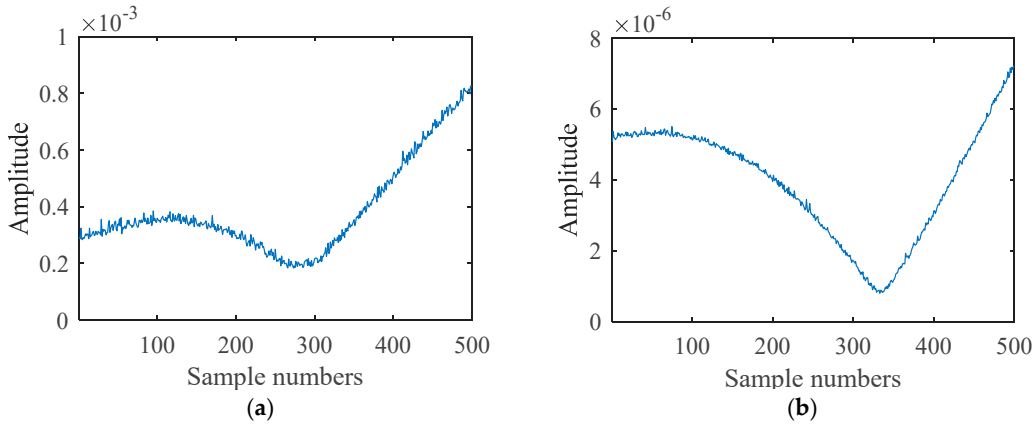

Figure 7. A sample example in difficult cases. (**a**) A sample of stripmap SAR; (**b**) a sample of spotlight SAR.

3.2. Method of SAR Mode Identification

This subsection discusses the overall scheme for SAR operating mode identification. The scheme of the SAR operating mode identification based on deep learning mainly includes two parts: multi-mode SAR sample generation and operating mode identification based on a neural network. Firstly, the samples are extracted in batches from the SAR signal database generated by simulation, and then the samples are input into the neural network for training. Finally, the pre-trained network is used to precisely predict the SAR operating mode.

The key parameters (usually including pulse duration, the linear FM rate, and so on) of the SAR signal are first estimated by the fractional Fourier transform (FrFT) algorithm. FrFT is a linear transformation on the time-frequency plane by rotating the time axis and the frequency axis counterclockwise at a certain angle [39–42]. Chirp signals with a fixed frequency-modulated rate will have an energy peak in a certain fractional domain. Therefore, FrFT can be used to detect chirp signals from white noise and estimate intra-pulse parameters.

If the estimated signal bandwidth is less than the preset threshold for GMTI, then the signal can be judged to be GMTI mode. Otherwise, we extracted the matrix of the amplitude peak of the signal and then input the matrix into the pre-trained neural network to identify the operating mode. The overall framework of the spaceborne SAR operating mode identification system is shown in the figure below (Figure 8).

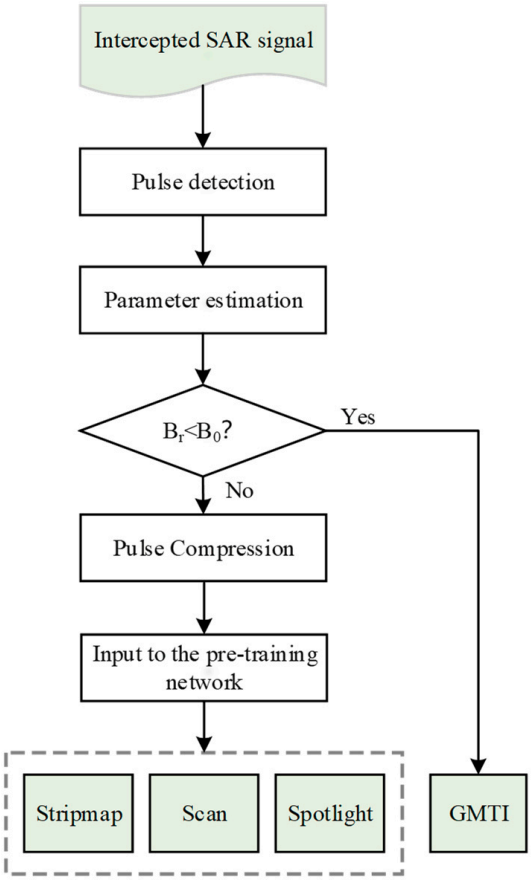

Figure 8. The workflow of the proposed SAR operating mode identification method.

4. Simulation and Analysis

In this section, the robustness of the proposed method to SNR, the jammer's position, and the number of the accumulated pulses is discussed in detail. In the experiment, a large number of training samples are generated based on the parameters of several typical spaceborne SAR. These parameters mainly include satellite orbital altitude, transmitting carrier frequency, antenna size, and received signal-to-noise ratio. As a result, 3600 train set samples were generated for each of the three operating modes of stripmap, scan, and spotlight. The specific parameter-setting ranges for the train set are shown in the following table (Table 1).

Table 1. Range of train set parameters.

Parameter	Value	Step−Size
Range antenna length	0.75 m, 1.5 m, 2.5 m	
Azimuth antenna length	9 m~15 m	1.5 m
Carrier frequency	1.25 GHz, 5.4 GHz, 9.6 GHz	
Bandwidth	10 MHz~30 MHz	10 MHz
Platform height	736 km~770 km	37.75 m
Elevation angle	10°~20°	5°
Squint angle	0°~4°	1°
Number of sub-swaths for scan SAR	4~6	1
Azimuth coordinates of jammer [1]	1 km~2 km	1 km
Ground range coordinates of jammer	40 km~80 km	40 km
SNR	6 dB~15 dB	3 dB

[1] The azimuth coordinates and ground range coordinates of the jammer are shown in Figure 2.

The other parameters used to generate echoes are set to fixed values, as shown in the following table (Table 2).

Table 2. The fixed parameters.

Parameter	Value
Pulse duration	40 μs
SAR transmitting power	1.5 kW
SAR antenna gain peak	40 dB
Jammer antenna gain peak	20 dB
SAR transmitting loss	2 dB
Jammer receiving loss	2 dB
Jammer load impedance	50 Ω
Jammer sampling frequency	120 MHz

The simulation uses the back propagation (BP) neural network, which is set as a four-layer network model. The feature numbers of each layer are, respectively, 1000, 100, 25, and 3. The network structure is shown in the following figure (Figure 9).

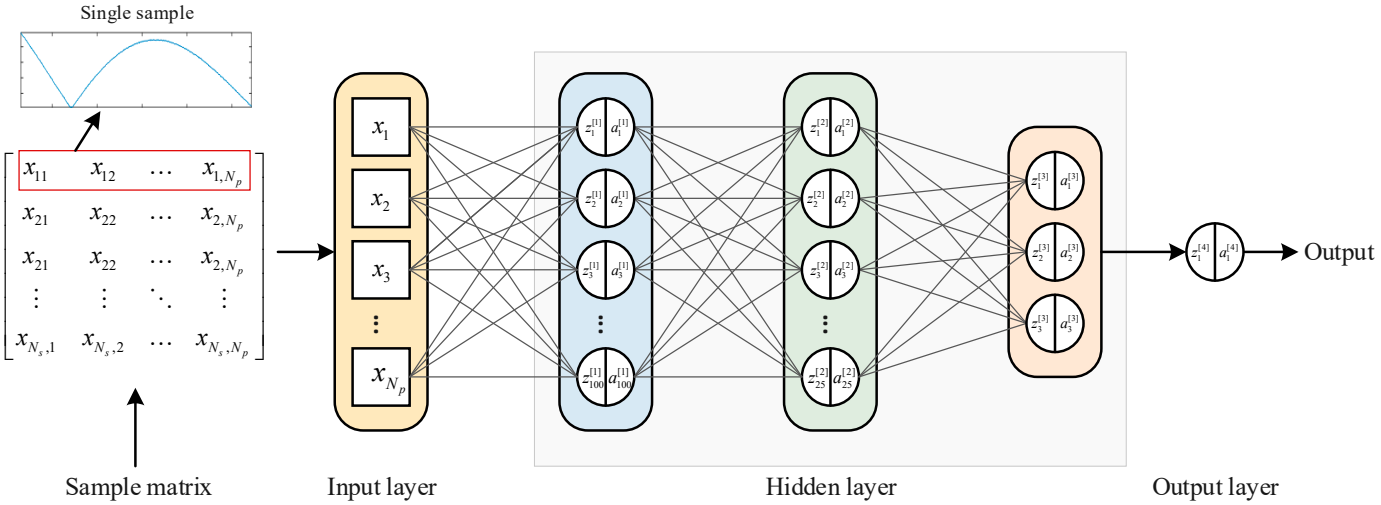

Figure 9. The structure of the BP neural network, where 'N_s' denotes the number of the samples and 'N_p' denotes the number of the accumulated pulses per sample.

The learning rate is set to 0.00001; the Adam optimizer and early-stopping is adopted; and the batch size is set to 32. With the increase in epoch number, the prediction accuracy of the train set and the test set is gradually improved, and the experimental results show that the accuracy tends to be stable when the number of iterations reaches 2000.

In the experiment, accuracy and cost are used to describe the training process of the neural network model. The accuracy denotes the prediction accuracy of the pre-trained model for the test set. The accuracy can be expressed as

$$Accuracy = \frac{TP_A + TP_B + TP_C}{N_{test}}, \tag{17}$$

where TP_A, TP_B, and TP_C denote the number of times that both the predicted result and the actual sample type are stripmap, scan, and spotlight, respectively; N_{test} denotes the number of samples in the test set.

The cost is an important parameter that determines how well a machine learning model performs for a given train set. Generally, the smaller the function value, the better the model fits. The cost can be expressed as

$$Cost = -\frac{1}{N_{train}} \sum_{i=1}^{N_{train}} \left[y^{(i)} \log \hat{y}^{(i)} + \left(1 - y^{(i)}\right) \log\left(1 - \hat{y}^{(i)}\right) \right], \tag{18}$$

where N_{test} denotes the number of samples in the train set; $y^{(i)}, i = 1, 2, \ldots, N_{train}$ denotes the label value of the i-th sample; and $\hat{y}^{(i)}, i = 1, 2, \ldots, N_{train}$ denotes the value that the model classifier predicts for the i-th sample.

4.1. Effect of SNR on Identification Accuracy

SNR is the primary factor that affects the identification accuracy. The signal will be submerged in the noise when the noise power is too high compared with the SAR signal power. In this subsection, simulation experiments are conducted on the identification accuracy for different receiving SNRs. In the following experiments, SNR is defined as the ratio of the average SAR signal power to the average noise power during jammer sampling. The specific parameter-setting ranges for the test set are shown in the following table (Table 3). Besides, the other parameters are kept the same as in the process of the train set production, and 108 samples are generated for each operating mode, respectively.

Table 3. Range of test set parameters.

Parameter	Value	Step−Size
Range antenna length	1 m~2 m	0.5 m
Azimuth antenna length	10 m~15 m	2.5 m
Carrier frequency	1.25 GHz~9.6 GHz	4.2 GHz
Bandwidth	10 MHz~30 MHz	10 MHz
Platform height	736 km~770 km	37.75 m
Elevation angle	12.5°~20°	7.5°
Squint angle	1°~3°	1°
Number of sub-swaths for scan SAR	4~6	2
Azimuth coordinates of jammer	2 km	
Ground range coordinates of jammer	80 km	
SNR	−8 dB~12 dB	4 dB

In the experiment, the train set containing 10,800 samples and the test set containing 324 samples were input into the network, where the train set and the test set have the same number of samples for stripmap, scan, and spotlight. When the number of the training epochs is set to 2000, the accuracy for the train set and the loss curve are shown in the figure below (Figure 10).

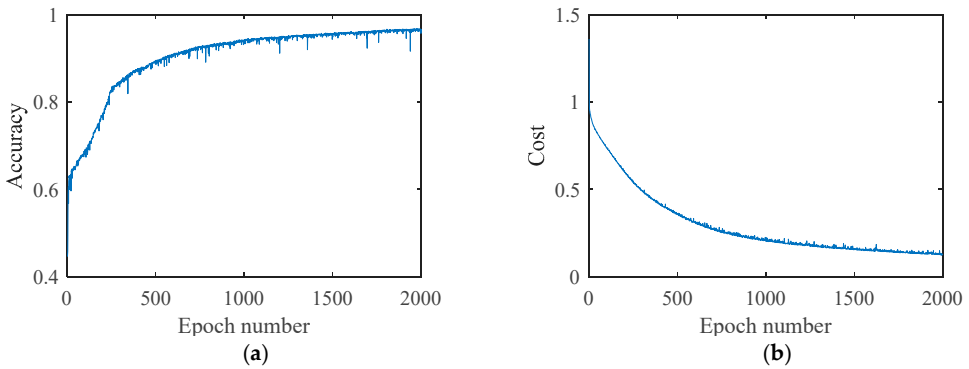

Figure 10. Curve diagram of training accuracy and loss. (**a**) Training accuracy curve; (**b**) training loss curve.

In the process of producing the test set, the SNR is set from −8 dB to 12 dB and the step-size is set to 4 dB. The prediction accuracy of the pre-trained network for each test set is shown in the table below (Table 4).

Table 4. The prediction accuracy for different SNRs.

SNR	−8 dB	−4 dB	0 dB	4 dB	8 dB	12 dB
Accuracy (this method)	75.62%	80.86%	85.49%	87.04%	88.58%	88.89%

As shown in the table above, the average prediction accuracy rate can reach 85% when the SNR is set above 0 dB. However, the identification accuracy apparently decreases with the reduction of SNR, especially when the SNR is less than 0 dB.

When the SNR is set to 12 dB, the classification confusion matrix of the method proposed in this paper is shown in the figure below (Figure 11).

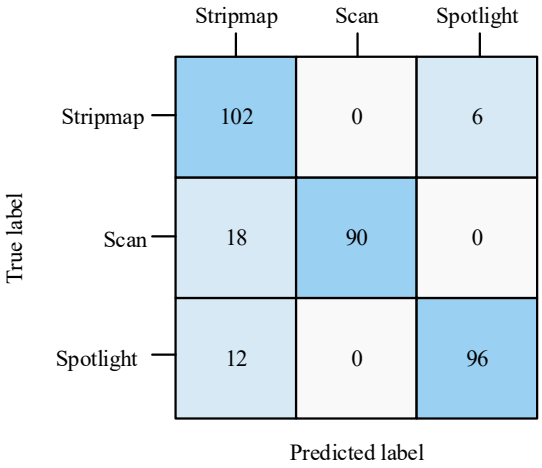

Figure 11. Classification confusion matrix of the method proposed in this paper.

As shown in the above figure, stripmap samples are easier to identify than scan or spotlight samples. At the same time, scan and spotlight samples are more likely to be misidentified as stripmap samples. Two sample cases of misidentification are shown in the figure below (Figure 12). We found that when the signal power is too low, which is usually due to the intercepted signal being in the low-gain area of the antenna pattern, the difficulty of identification will be increased. In this regard, we can deploy several jammers at different locations (generally along the azimuth) to ensure that the intercepted signal power is high enough.

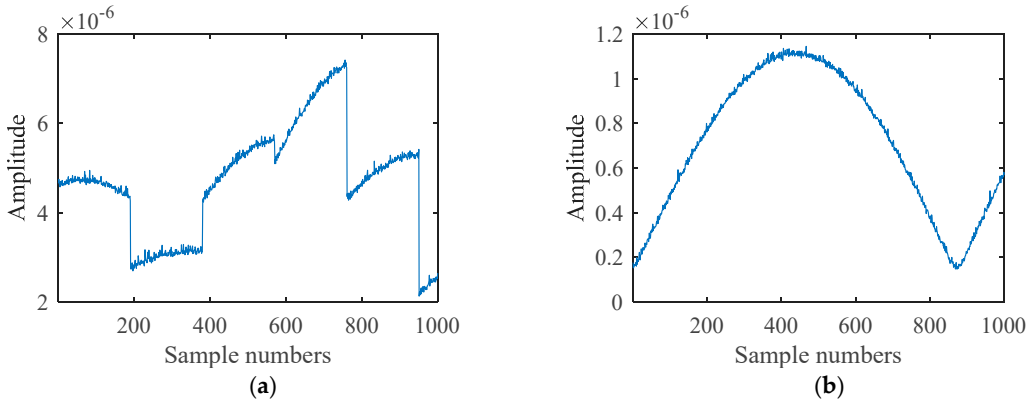

Figure 12. Sample cases of misidentification. (**a**) Scan sample; (**b**) spotlight sample.

Since the proposed method is based on sidelobe reconnaissance, the signal experiences sidelobe decay. In order to compensate for the case of low SNR, we further consider using a matching filter to enhance the peak signal-to-noise ratio (PSNR), and the compressed signals are used to make a mode identification. To this end, the fractional Fourier transform (FrFT) algorithm is employed to obtain the required parameters. The detailed process to obtain the filter is as follows.

First, pulse detection is performed and then some intra-pulse parameters such as pulse duration and pulse repetition interval (PRI) can be estimated [43]. Then, we extract the first several pulses intercepted and estimate the frequency-modulated rate by the FrFT algorithm so that pulse compression can be performed.

The amplitude of a section of intercepted signal before and after pulse compression is shown in the figure below (Figure 13).

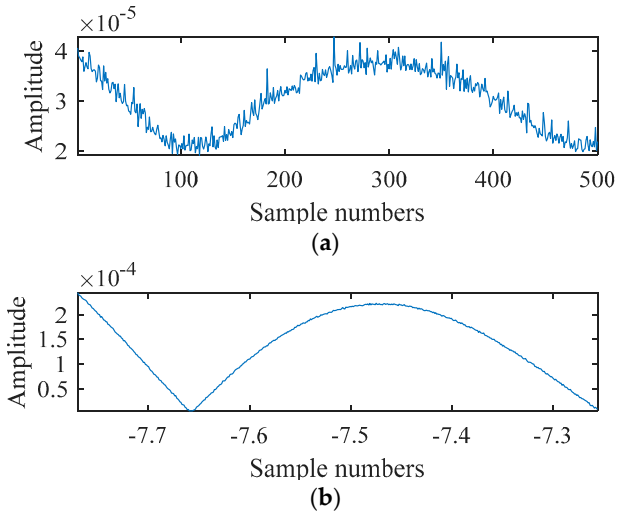

Figure 13. The amplitude of the signal before and after pulse compression. (**a**) Before pulse compression; (**b**) after pulse compression.

The data set with pulse compression is trained and predicted with other settings being unchanged. When the number of epochs is set to 2000, the accuracy for the train set and the loss curve are shown in the figure below (Figure 14).

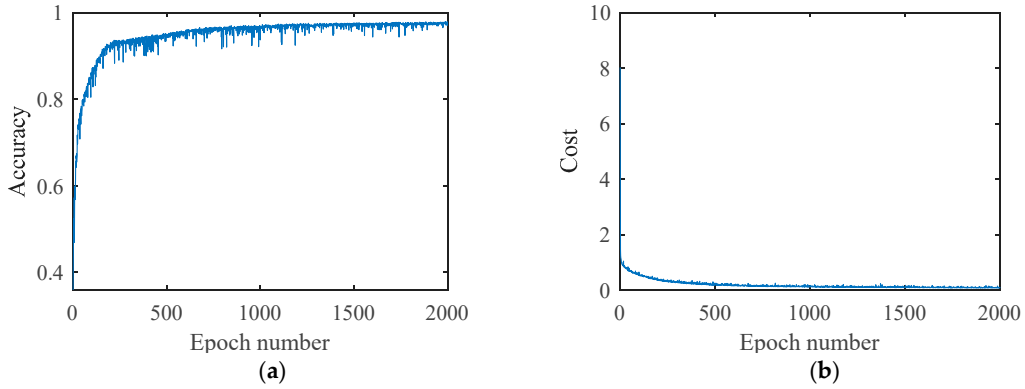

Figure 14. Curve diagram of training accuracy and loss. (**a**) Training accuracy curve; (**b**) training loss curve.

Clearly, the network with pulse compression obtains an improved convergence rate which results from a higher SNR. In the process of producing the test set, the SNR is set from −8 dB to 12 dB and the step-size is set to 4 dB. The prediction accuracy of the pre-trained network with pulse compression as well as the method proposed in [32] for each test set is shown in the table below (Table 5).

Table 5. The prediction accuracy with pulse compression for different SNRs.

SNR	−8 dB	−4 dB	0 dB	4 dB	8 dB	12 dB
Accuracy	89.81%	91.67%	91.67%	90.74%	90.43%	91.36%
Accuracy [32]	77.16%	82.10%	84.57%	86.73%	87.35%	88.58%

As shown in the table above, when the SNR is lower than 12 dB and higher than −8 dB, the identification accuracy rate remains at about 90% and will not deteriorate rapidly with the decrease in SNR. Therefore, the method based on the FrFT estimation algorithm can cope with the situation of poor SNR.

A Gated Recurrent Unit (GRU) neural network, an improved recurrent neural network, is employed in [32]. The experimental results show that the accuracy of the proposed method is slightly higher than the method employed in [32] when the SNR is higher than 0 dB; but, the accuracy of the method with pulse compression is much higher than the method employed in [32].

When the SNR is set to 12 dB, the classification confusion matrix of the method with pulse compression is shown in the figure below (Figure 15).

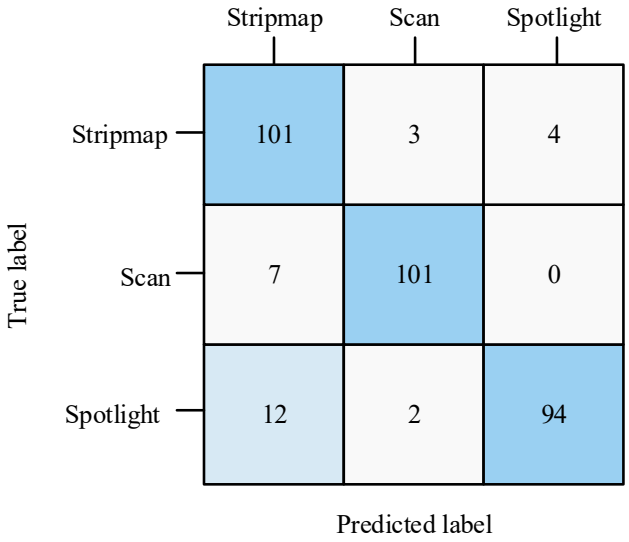

Figure 15. Classification confusion matrix of the method with pulse compression.

As shown in the above figure, compared with Figure 11, the identification accuracy has been improved. Similarly, scan and spotlight samples are more likely to be misidentified as stripmap samples.

4.2. Effect of the Jammer Position

Considering that the relative position of the jammer is unpredictable and uncontrollable when intercepting SAR signals, this subsection will verify the robustness of this method to the uncertainty of the relative position of the jammer.

A part of the antenna pattern in azimuth for the point target is shown in the figure below (Figure 16). In the experiment, three typical jammer positions are selected along the azimuth as marked in the figure below (Figure 16). Specifically, among them, one is placed at the peak of the first sidelobe, one at the trough between the main lobe and the first sidelobe, and one at the midpoint between the former two.

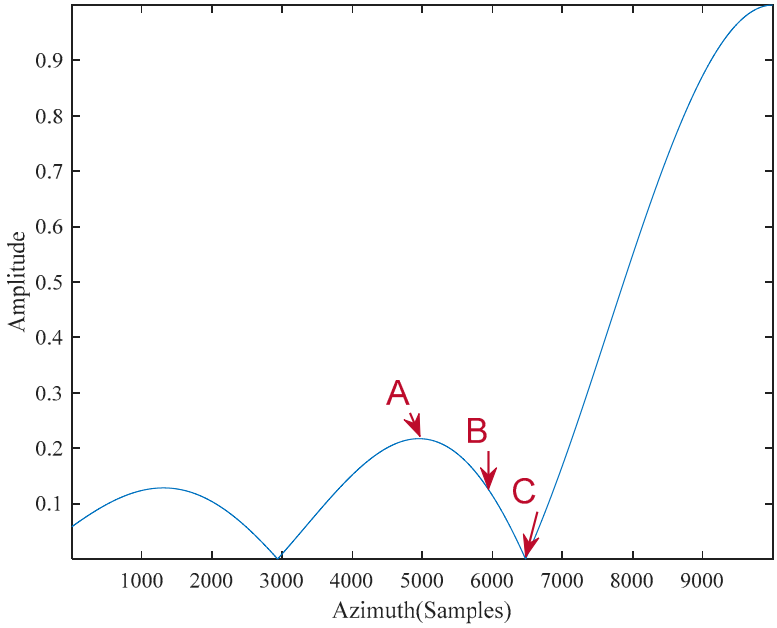

Figure 16. The antenna pattern in the azimuth plane for the point target.

Three jammers are placed at A, B, and C, respectively, as shown in the figure above, the SNR is set to 12 dB, and other settings are consistent with the experiment in Section 4.1. The training results are shown in the following table (Table 6).

Table 6. The prediction accuracy when the jammer is set at points A, B, and C, respectively.

Without Pulse Compression		**With Pulse Compression**	
Position	**Accuracy**	**Position**	**Accuracy**
A	91.05%	A	95.06%
B	89.51%	B	93.83%
C	86.73%	C	92.28%

Apparently, when the jammer is deployed at the above three typical positions, the identification accuracy rate can maintain itself above 86% and the rate can reach above 90% when pulse compression is employed. Hence, the robustness of this method to the jammer position is verified experimentally.

4.3. Effect of the Number of the Accumulated Pulses

The number of accumulated pulses required is closely related to the identification speed. As the number of accumulated pulses increases, the identification accuracy will increase, while the time required for identification will also increase. If an acceptable identification accuracy can be obtained with fewer pulses, the reconnaissance system for the SAR operating mode will be much more efficient. Therefore, this subsection discusses the relationship between the number of accumulated pulses and identification accuracy, so as to obtain an empirical optimal accumulated pulse number, which can provide a reference for future engineering application.

The following experiments set the number of the intercepted pulses from 100 to 1000, respectively, and the SNR is set to 12 dB while other experimental settings are consistent with Section 4.1. The experimental results are shown in the table below (Table 7).

Table 7. Accuracy results for the different numbers of accumulated pulses.

Without Pulse Compression		With Pulse Compression	
Np	**Accuracy**	**Np** [1]	**Accuracy**
1000	88.89%	1000	91.36%
900	89.81%	900	87.35%
800	87.96%	800	88.89%
700	87.35%	700	88.27%
600	87.04%	600	90.12%
500	82.10%	500	87.96%
400	81.48%	400	87.65%
300	79.32%	300	81.79%
200	71.91%	200	78.09%
100	57.41%	100	63.58%

[1] 'Np' denotes the number of the accumulated pulses.

The experimental results show that without pulse compression, the identification accuracy will become less than 85% when the accumulated pulse number is reduced to 500. Furthermore, with the reduction of the accumulated pulse number, the accuracy will decrease sharply. With pulse compression employed, the accuracy can still remain above 85% when the pulse number is reduced to 400.

In order to balance the identification accuracy and the speed, it is appropriate to set the accumulated pulse number to 600 without pulse compression. Besides, the number can be set to 400 with pulse compression employed.

5. Conclusions

To solve the problem of SAR operating mode identification, an intelligent model based on sidelobe reconnaissance and machine learning is proposed in this paper. This method uses the SAR signal intercepted by the ground-based jammer as the input and can identify four operating modes (stripmap, scan, spotlight, and GMTI). The method takes account of both identification accuracy and speed, and it has good robustness to low SNR and uncertainty of the jammer's position. Furthermore, pulse compression can be employed to improve the robustness to low SNR. Finally, the experimental results show that the method can maintain satisfactory performance even if the accumulated pulse number is reduced to 400 when pulse compression is employed. In the future, in order to cope with complex electromagnetic environments and the development of radar technologies, we will further discuss some better machine learning algorithms to improve the employed model in this paper.

Author Contributions: Conceptualization, R.M.; methodology, R.M. and G.J.; validation, C.S. and Y.W.; formal analysis, G.J. and R.M.; investigation, R.M. and C.S.; writing—original draft preparation, R.M.; writing—review and editing, Y.L. and D.Z. All authors have read and agreed to the published version of the manuscript.

Funding: This work was supported by the National Natural Science Foundation of China (Grant No. 62101248), the Natural Science Foundation of Jiangsu Province (Grant No. BK20210282), the Shenzhen Science and Technology Program (Grant No. JCYJ20230807142000001), the Fundamental Research Funds for the Central Universities (Grant No. NT2023008), the China Postdoctoral Science Foundation (Grant No. 2022M711542), and the 2021 Jiangsu Shuangchuang (Mass Innovation and Entrepreneurship) Talent Program (Grant No. JSSCBS20210164).

Data Availability Statement: Data are contained within the article.

Acknowledgments: The authors would like to express their gratitude to the anonymous reviewers and the associate editor for their constructive comments on this paper.

Conflicts of Interest: The authors declare no conflicts of interest.

References

1. Cheney, M. A mathematical tutorial on synthetic aperture radar. *SIAM Rev.* **2001**, *43*, 301–312. [CrossRef]
2. Deng, Y.; Yu, W.; Zhang, H.; Wang, W.; Liu, D.; Wang, R. Forthcoming Spaceborne SAR Development. *J. Radars* **2020**, *9*, 1–33.
3. Moreira, A.; Prats-Iraola, P.; Younis, M.; Krieger, G.; Hajnsek, I.; Papathanassiou, K.P. A tutorial on synthetic aperture radar. *IEEE Geosci. Remote Sens. Mag.* **2013**, *1*, 6–43. [CrossRef]
4. Ouchi, K. Recent Trend and Advance of Synthetic Aperture Radar with Selected Topics. *Remote Sens.* **2013**, *5*, 716–807. [CrossRef]
5. Jin, G.; Wang, Y.; Zhu, D.; Niu, S.; Yan, H. A Reconfigurable MIMO-SAR Transmission Scheme Based on Inter-Pulse and Intra-Pulse Joint Phase Modulation. *IEEE Trans. Signal Process.* **2022**, *70*, 4265–4276. [CrossRef]
6. Gan, R.-b.; Wang, J.-g. Improvement of the responsive deception for spaceborne SAR. *J. Univ. Electron. Sci. Technol. China* **2005**, *34*, 614–617.
7. Liu, Y.; Wang, W.; Pan, X.; Xu, L.; Wang, G. Influence of Estimate Error of Radar Kinematic Parameter on Deceptive Jamming Against SAR. *IEEE Sens. J.* **2016**, *16*, 5904–5911. [CrossRef]
8. Paine, A.S. An adaptive beamforming technique for countering synthetic aperture radar (SAR) jamming threats. In Proceedings of the 2007 IEEE Radar Conference, Waltham, MA, USA, 17–20 April 2007; pp. 630–634.
9. Sun, Q.; Shu, T.; Thou, S.; Tang, B.; Yu, W. A Novel Jamming Signal Generation Method for Deceptive SAR Jammer. In Proceedings of the 2014 IEEE Radar Conference, Rome, Italy, 8–10 October 2014; pp. 1174–1178.
10. Sun, Q.; Shu, T.; Yu, K.-B.; Yu, W. Efficient Deceptive Jamming Method of Static and Moving Targets Against SAR. *IEEE Sens. J.* **2018**, *18*, 3610–3618. [CrossRef]
11. Cheng, Y.; Zhu, D.; Jin, G.; Zhang, J.; Niu, S.; Wang, Y. A Novel Intrapulse Repeater Mainlobe-Jamming Suppression Method with MIMO-SAR. *IEEE Geosci. Remote Sens. Lett.* **2022**, *19*, 4507805. [CrossRef]
12. Wang, Y.; Jin, G.; Song, C.; Lu, P.; Han, S.; Lv, J.; Zhang, Y.; Wu, D.; Zhu, D. Parameterized and Large-dynamic-range Two-dimensional Precise Controllable SAR Jamming: Characterization, Modeling, and Analysis. *IEEE Trans. Geosci. Remote Sens.* **2023**, *61*, 5209416.
13. Huang, B.; Wang, W.-Q.; Zhang, S.; Wang, H.; Gui, R.; Lu, Z. A Novel Approach for Spaceborne SAR Scattered-Wave Deception Jamming Using Frequency Diverse Array. *IEEE Geosci. Remote Sens. Lett.* **2020**, *17*, 1568–1572. [CrossRef]
14. Sun, Q.; Shu, T.; Yu, K.-B.; Yu, W. A Novel Deceptive Jamming Method Against Two-Channel SAR-GMTI Based on Two Jammers. *IEEE Sens. J.* **2019**, *19*, 5600–5610. [CrossRef]
15. Zhao, B.; Huang, L.; Zhou, F.; Zhang, J. Performance Improvement of Deception Jamming Against SAR Based on Minimum Condition Number. *IEEE J. Sel. Top. Appl. Earth Obs. Remote Sens.* **2017**, *10*, 1039–1055. [CrossRef]
16. Zhao, B.; Zhou, F.; Bao, Z. Deception Jamming for Squint SAR Based on Multiple Receivers. *IEEE J. Sel. Top. Appl. Earth Obs. Remote Sens.* **2015**, *8*, 3988–3998. [CrossRef]
17. HanYan, L.I.U.; HongJun, S.; ZengJu, C. Comparative study on stripmap mode, spotlight mode, and sliding spotlight mode. *J. Grad. Sch. Acad. Sci.* **2011**, *28*, 410–417.
18. Bin, D.; Yuliang, Q.; Yanpeng, L.; Hongqiang, W.; Xiang, L. Fast simulation of raw signals from natural scenes for squint stripmap SAR. In Proceedings of the 2009 2nd Asian-Pacific Conference on Synthetic Aperture Radar (APSAR 2009), Xi'an, China, 26–30 October 2009; pp. 235–238.
19. Chen, J.; Wang, K.; Yang, W.; Liu, W. Accurate Reconstruction and Suppression for Azimuth Ambiguities in Spaceborne Stripmap SAR Images. *IEEE Geosci. Remote Sens. Lett.* **2017**, *14*, 102–106. [CrossRef]
20. Dogan, O.; Kartal, M. Efficient Stripmap-Mode SAR Raw Data Simulation Including Platform Angular Deviations. *IEEE Geosci. Remote Sens. Lett.* **2011**, *8*, 784–788. [CrossRef]
21. Mao, X.H.; Zhu, D.Y.; Zhu, Z.D. Signatures of Moving Target in Polar Format Spotlight SAR Image. *Prog. Electromagn. Res.* **2009**, *92*, 47–64. [CrossRef]
22. Mittermayer, J.; Lord, R.; Bömer, E. Sliding spotlight SAR processing for TerraSAR-X using a new fon-nulation of the extended chirp scaling algorithm. In *Proceedings: Learning from Earth's Shapes And Sizes, Proceedings of the IGARSS 2003: IEEE International Geoscience and Remote Sensing Symposium*; IEEE: New York, NY, USA, 2003; Volumes I–VII, pp. 1462–1464.
23. Mittermayer, J.; Moreira, A.; Loffeld, O. Spotlight SAR data processing using the frequency scaling algorithm. *IEEE Trans. Geosci. Remote Sens.* **1999**, *37*, 2198–2214. [CrossRef]
24. Zhu, D.; Ye, S.; Zhu, Z. Polar Format Algorithm using Chirp Scaling for Spotlight SAR Image Formation. *IEEE Trans. Aerosp. Electron. Syst.* **2008**, *44*, 1433–1448. [CrossRef]
25. Bamler, R.; Eineder, M. ScanSAR processing using standard high precision SAR algorithms. *IEEE Trans. Geosci. Remote Sens.* **1996**, *34*, 212–218. [CrossRef]
26. Holzner, J.; Bamler, R. Burst-mode and ScanSAR interferometry. *IEEE Trans. Geosci. Remote Sens.* **2002**, *40*, 1917–1934. [CrossRef]
27. Jin, M.Y. Optimal range and Doppler centroid estimation for a ScanSAR system. *IEEE Trans. Geosci. Remote Sens.* **1996**, *34*, 479–488. [CrossRef]
28. Li, N.; Wang, R.; Deng, Y.; Chen, J.; Zhang, Z.; Liu, Y.; Xu, Z.; Zhao, F. Improved Full-Aperture ScanSAR Imaging Algorithm Based on Aperture Interpolation. *IEEE Geosci. Remote Sens. Lett.* **2015**, *12*, 1101–1105. [CrossRef]
29. Chen, Y.; Wu, Y.; Jia, X. Surveillance study of spaceborne synthetic aperture radar in different working modes. *Comput. Eng. Appl.* **2013**, *49*, 223–227.

30. Tang, X.; Li, C.; Sun, B. Inversion method of spaceborne SAR operating mode based on genetic algorithm. *Space Electron. Technol.* **2013**, *10*, 90–94.
31. Xia, Z.; Zhong, H.; Chen, W. Identification of spaceborne SAR operating mode in reconnaissance mode. *J. Hangzhou Dianzi Univ. (Nat. Sci.)* **2017**, *37*, 36–40. [CrossRef]
32. He, J.; Zhang, Y.-S.; Yin, C.-B. Operating modes identification of spaceborne SAR based on deep learning. *J. Zhejiang Univ. (Eng. Sci.)* **2022**, *56*, 1676–1684.
33. Ioffe, S.; Szegedy, C. Batch Normalization: Accelerating Deep Network Training by Reducing Internal Covariate Shift. In Proceedings of the International Conference on Machine Learning, Lille, France, 6–11 July 2015; Volume 37, pp. 448–456.
34. Olkhovskiy, M.; Mullerova, E.; Martinek, P. Impulse signals classification using one dimensional convolutional neural network. *J. Electr. Eng.-Elektrotechnicky Cas.* **2020**, *71*, 397–405. [CrossRef]
35. Qu, W.; Wu, Y.; Jia, X. Study on SAR Antenna Side Lobe Reconnaissance. *J. Acad. Equip. Command. Technol.* **2004**, *15*, 103–107.
36. Bachmann, M.; Schwerdt, M.; Braeutigam, B. Accurate Antenna Pattern Modeling for Phased Array Antennas in SAR Applications-Demonstration on TerraSAR-X. *Int. J. Antennas Propag.* **2009**, *2009*, 492505. [CrossRef]
37. Kim, S.Y.; Sung, J.B.; Torre, A. In-Orbit Antenna Pattern Extraction Method for Active Phased-Array SAR Antennas. *IEEE Antennas Wirel. Propag. Lett.* **2016**, *15*, 317–320. [CrossRef]
38. Shimada, M.; Freeman, A. A Technique for Measurement of Spaceborne Sar Antenna Patterns Using Distributed Targets. *IEEE Trans. Geosci. Remote Sens.* **1995**, *33*, 100–114. [CrossRef]
39. Candan, Ç.; Kutay, M.A.; Ozaktas, H.M. The discrete fractional Fourier transform. *IEEE Trans. Signal Process.* **2000**, *48*, 1329–1337. [CrossRef]
40. Ozaktas, H.M.; Ankan, O.; Kutay, M.A.; Bozdagi, G. Digital computation of the fractional Fourier transform. *IEEE Trans. Signal Process.* **1996**, *44*, 2141–2150. [CrossRef]
41. Pei, S.C.; Yeh, M.H.; Tseng, C.C. Discrete fractional Fourier transform based on orthogonal projections. *IEEE Trans. Signal Process.* **1999**, *47*, 1335–1348. [CrossRef]
42. Xinghao, Z.; Ran, T.; Bing, D. Practical Normalization methods in the digital computation of the fractional Fourier transform. In Proceedings of the 2004 7th International Conference on Signal Processing Proceedings, Beijing, China, 31 August–4 September 2004; Volumes 1–3, pp. 105–108.
43. Wang, Y. Research on the Modulation Recognition Algorithms and Parameter Estimation Algorithms of Radar Signal. Master's Thesis, National University of Defense Technology, Changsha, China, 2012.